First principles molecular dynamics calculations of the mechanical properties of endofullerenes containing noble gas atoms or small molecules

Laurent Pizzagalli

Journal Name

ARTICLE TYPE

Cite this: DOI: 00.0000/xxxxxxxxxx

First principles molecular dynamics calculations of the mechanical properties of endofullerenes containing noble gas atoms or small molecules†

Laurent Pizzagalli[a]

Received Date
Accepted Date

DOI: 00.0000/xxxxxxxxxx

The mechanical properties of endofullerenes have been investigated by performing compression tests using finite temperature first principles molecular dynamics calculations. We considered various X@C_{60} systems, with X a single noble gas atom (He, Ne, Ar, Kr, or Xe), small molecules (H_2O, CH_4), or small helium clusters. In the absence of compression, it is observed that there is no or at best a negligible effect of X on the properties of C_{60}. The compression simulations revealed several original findings. First, the influence of X on the stiffness of X@C_{60} can be quantified, although it is at most 12% for the studied cases. Next, both energy and contact force variations as a function of strain are demonstrated to depend on X. However, this is not the case for the yield strain and for the failure mechanism of the C_{60} shell. Finally, it is shown that the X@C_{60} compression could bring X to be in a high stress state. In the specific cases of H_2O and CH_4 molecules, a mechanism of stress assisted dissociation is observed.

1 Introduction

Endohedral fullerenes or endofullerenes are closed shell fullerenes encapsulating atoms, molecules or clusters. They can be synthesized using several techniques, among which high pressure incorporation or molecular beam implantation.[1–3] For instance, the former approach allowed to achieve the incorporation of noble gas atoms.[4–7] More recently, Kurotobi and Murata developed a molecular surgery technique to open a C_{60}, insert a water molecule, and close up the carbon shell.[8] Bloodworth et al. used a related approach to trap a noble gas atom or a methane molecule into C_{60}.[9,10]

Studying endofullerenes is interesting and important in several ways. A first incentive would be the controlled modification of properties caused by the presence of the guest molecule or cluster. For example let us consider mechanical properties, which are nowadays satisfactorily understood for the empty C_{60}, thanks to several dedicated studies.[11–16] We know that C_{60} is a resilient molecule,[17] which can sustain a huge elastic deformation up to about 48%.[16] For larger compression strains, the yielding of the C_{60} shell by bond breaking is observed, but a perfect or weakly defected structure can be recovered by unloading if the strain does not exceed 75%. It is rational to assume that introducing one or several atoms inside the C_{60} shell could change this picture, especially at large deformations. For instance, an endofullerene could probably be stiffer than the empty fullerene. Also, both the yield stress and the plasticity mechanisms could be affected.

A promising feature of endofullerenes is that they provide a unique mean to encapsulate and isolate a single atom or molecule, opening the way to potential applications in memory storage or quantum computations,[18] or to investigate the intrinsic properties of the trapped guest. The properties and characteristics of the latter could also be modified by applying an external perturbation on the endofullerene. For instance, on the basis of first-principles calculations, Sabirov and co-workers predicted that the dissociation of a trapped H_2O or CH_4 molecule could be achieved by the compression of the C_{60} host.[19,20] Futhermore squeezing the C_{60} shell leads to a reduction of its internal volume, which could potentially put a single atom in a high pressure state.

The last decades have witnessed an impressive development of experimental apparatus allowing to probe mechanical properties of matter at the nanoscale.[21,22] For instance the controlled compression of single nanoparticles with a size equal to a few tens of nm has been achieved.[23–27] However, systems as small as fullerenes or endofullerenes remain out of reach of the current capabilities. Note that scanning probe techniques have been successfully used to probe the mechanical properties of C_{60}, but that these investigations are restricted to a low deformation regime.[28,29] Numerical simulations are often a useful complement or substitute to experiments, and a large number of classical

[a] Institut P', CNRS UPR 3346, Université de Poitiers, SP2MI, Boulevard Marie et Pierre Curie, TSA 41123, 86073 Poitiers Cedex 9, France. E-mail: Laurent.Pizzagalli@univ-poitiers.fr

† Electronic Supplementary Information (ESI) available: [details of any supplementary information available should be included here]. See DOI: 10.1039/cXCP00000x/

molecular dynamics calculations have been devoted to determine the mechanical properties of nanoparticles (for a recent review see Ref.[30]). Critical issues are however the lack of available classical interatomic potentials for multicomponents systems or their questionable reliability at the nanoscale and for large deformations. To overcome this hurdle, we have recently developed a numerical approach allowing for the compression of nano-objects at finite temperature by combining first principles MD calculations with classical force fields. In the present study, this approach is applied to investigate the properties of $X@C_{60}$ endofullerenes under compression. Several X guests are considered: single noble gas atoms from He to Xe, clusters of He atoms, and methane and water molecules.

This paper is structured as follows. In the section 2 the setup of the simulations is described with all details provided. The section 3 is dedicated to the structure and stability of the endofullerenes at room temperature. Their mechanical properties are described in the section 4. Finally the section 5 is dedicated to the state of the atoms and molecules encapsulated into the compressed C_{60} shell. Our conclusions are gathered in the final section.

2 Methods

2.1 First principles molecular dynamics calculations

First principles MD calculations are performed using the Car-Parrinello method[31] implemented in the Quantum Espresso package.[32] We use a timestep of 0.2 fs, an effective electron mass of 600 a.u., and an electron mass cutoff of 5 Ry.[33] Ions and electrons are thermalized, using Nose-Hoover thermostats with oscillation frequencies of 90 THz for electrons and 30 THz for ions. The thermostat targets are an electronic kinetic energy of 0.005 a.u. for electrons and a temperature of 300 K for ions, respectively. These parameters were shown to be appropriate for C_{60} compression in a previous work.[15]

The electronic structure is calculated using density functional theory.[34,35] A good convergence is obtained with a plane waves basis cutoff of 25 Ry, except for systems including an oxygen ion for which a larger cutoff of 40 Ry is employed. The Perdew-Burke-Ernzerhof (PBE) functional is used to compute exchange-correlation contributions.[36] Interactions between ions and electrons are described with ultrasoft pseudopotentials.[37] All calculations are carried out using a cubic supercell with a length of 20 Å, which is large enough to prevent spurious interactions between the endofullerene and its periodic images.[15]

With these parameters, carbon bond lengths of 1.401 Å and 1.451 Å are obtained when the C_{60} structure is relaxed with a conjugate gradient energy minimization, in excellent agreement with the literature.[38]

2.2 Uniaxial compression

Two different sets of MD calculations are carried out. In the first one, each $X@C_{60}$ system is let free to evolve at 300 K for 20 ps. The first 10 ps are long enough to achieve thermalization. Different properties can then be extracted by averaging over the last 10 ps. These simulations are useful to determine the structure and the stability at 300 K, described in section 3.

In the second set, the uniaxial compression of each endofullerene is achieved by following the methodology described in details in Ref.[15], and only briefly reported here. Each system is orientated so that the z-axis, the compression axis by convention, passes through opposite pentagons in the C_{60} shell. In the MD simulations a repulsive quadratic force field acting on ions is activated. Atoms with z-coordinates above an upper threshold value are pushed down by the force field. Similarly, atoms with z-coordinates below a lower threshold value are pushed up. The upper (lower) threshold value is decreased (increased) at each time step, thus allowing for a continuous and smooth compression of the endofullerene. The chosen increment is 1×10^{-5} Å, yielding a compression speed of 0.1 Å/ps, which is typical of nanoparticles compression simulations.[14,30,39] The strength of the force field is set to 30 a.u., thus modeling an extremely stiff flat-punch indenter.

Both the total energy and the contact force are recorded at each MD step. The contact force is equal to half the sum of all repulsion contributions from the force field. Note that each pushed ion also experiences a friction force perpendicular to the compression axis and proportional to its mass, its velocity, and a parameter Γ equal to 500 a.u. This additional constraint hinders the free rotation of the quasi-spherical C_{60} shell during the compression.[15]

The engineering strain $\varepsilon = \delta d/d_0$ is used in this work, the reference length d_0 being determined for each system during the first set of MD calculations. Because of the small dimensions involved, the strain accuracy is estimated to be at best 1%. A typical MD compression run involves 2.2×10^5 iterations i.e., 44 ps. This is long enough to achieve compression strains up to 60%.

2.3 Bader volume and charge analysis

We also determine the Bader volume and charge of all atoms during the compression by performing an Atom in Molecule (AIM) analysis[40] using the CRITIC2 tool.[41] More precisely, the atomic structure is first extracted from the compression run for a selected configuration at a given time step. A separate self-consistent field calculation is next carried out using Quantum Espresso and the same parameters than in MD calculations. The only difference is that the ion-electron interactions are now calculated in the framework of the PAW method.[42] This allows for recovering the all-electrons density close to the nuclei, which is required for an accurate determination of the atomic basins in the AIM approach. Once this last step is achieved, per-atom quantities like the Bader volume V_B and the charge are computed by integration of the pseudo-density using the Yu-Trinkle algorithm,[43] and summed for each X guest. The charge is expressed as the excess number of electrons relative to the ground state. For instance, a value of $+0.19\ e^-$ for $He_{10}@C_{60}$ means an excess of 0.19 electrons carried by He_{10} (and then a deficit of 0.19 electrons for C_{60}). It is important to specify that the atomic volume cannot be unambiguously defined, and that AIM is only one method among others to perform a spatial decomposition. Variations of AIM-derived quantities like the atomic volume or the excess charge are useful indicators to monitor the systems during compression, but one should

not put too much weight on their absolute values.

3 Structure and stability

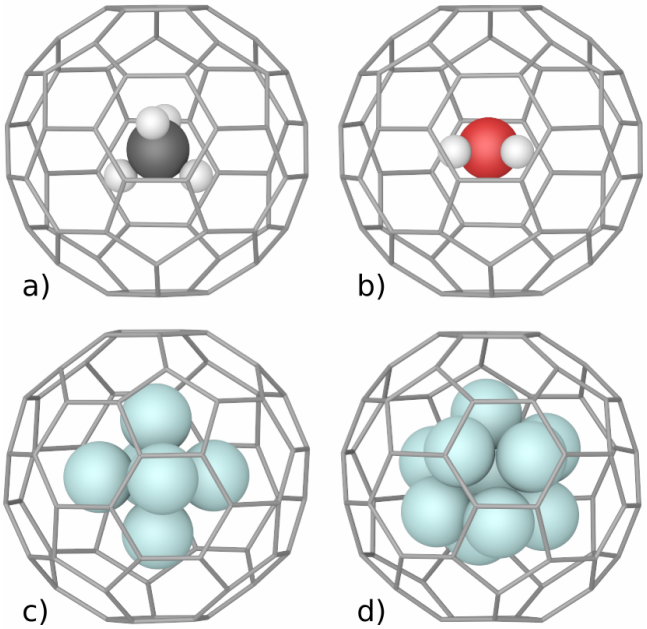

Fig. 1 Structures of a) CH_4@C_{60}, b) H_2O@C_{60}, c) He_6@C_{60}, and d) He_{10}@C_{60}. Ball-and-stick representations are used for guests, while only the carbon bonds of the C_{60} host are shown for clarity.

We first describe and discuss the structure and energetic stability at 300 K and with no compression, for all investigated systems. In the case of a single noble gas atom, it is generally agreed in the literature[51–53] that (i) the deformation of the C_{60} shell is negligible, (ii) the binding energy between X and C_{60} is small, equal to a few hundredths of eV at most in absolute value, (iii) its sign seems to be highly dependent on the calculation method, and (iv) the most stable structure retains the I_h symmetry with a centered noble gas atom. Our results are overall in accordance with these conclusions, with C_{60} shell dimensions changes Δd_H and Δd_P smaller than 0.01 Å and low binding energies (Tab. 1), and a noble gas at the C_{60} center. We find a negative binding energy i.e., an attractive interaction, only in the case of Xe@C_{60}. We emphasize that we do not aim at the same precision than in the previously published works, based on 0 K hybrid functional calculations with corrections for zero point energy and dispersion forces.[51–53] In the present study our accuracy is essentially limited by the finite temperature averaging and the use of the approximate PBE exchange-correlation functional. Note that we performed additional calculations including semi-empirical dispersion contributions,[54] which show that these corrections are negligible. Furthermore, as will be detailed in the following, the strain energies associated with mechanical compression are typically 2-3 orders of magnitude larger than the binding energies. Table 1 also reports the charge transfer ΔQ between X and C_{60} as estimated with the AIM approach. This charge transfer is found to be zero (He and Ne) or equivalent to a small electron deficit (Ar and Xe). The Kr case is puzzling with a transfer from X to C_{60} of 0.39 e^-, one order of magnitude larger than for other noble gas.

Considering CH_4, we find that the initial T_d symmetry of the molecule is preserved during 20 ps at 300 K, with the carbon atom located at the C_{60} center (Fig. 1-a). The C_{60} deformation is negligible, which may mean that the molecule is relatively free to rotate. However, rotation is barely observed during the 20 ps run, hinting at some directional interaction between C_{60} and CH_4. Our calculated binding energy is -0.789 eV (Tab. 1), i.e. the interaction is attractive. This appears to be slightly lower than the 0 K values reported in the literature.[55,56] There is no charge transfer between CH_4 and C_{60}. The C–H bond length in CH_4 is 1.098 Å in average at 300 K, in excellent agreement with previous works.[55] It is slightly lower than the computed bond length of 1.113 Å for the free CH_4 molecule, in agreement with a weak interaction with the C_{60} host.

Our calculations also show that the interaction between H_2O and C_{60} is minimal, with almost no perturbation of the C_{60} geometry (Tab. 1). The computed binding energy is close to zero, in agreement with results from Galano et al.[56] However, earlier investigations reported values ranging from -0.50 to -0.02 eV.[57,58] The encapsulated H_2O molecule retains the C_{2v} symmetry (Fig. 1-b), with a H–O bond length decrease of 0.004 Å and a $\widehat{HOH}$ angle increase of 0.22° compared to the free molecule at 300 K. Similar negligible changes are reported in the literature.[57,58] We also find that the O atom of the H_2O molecule remains close to the C_{60} center during the 300 K run, and that the molecule rotates easily as expected.[29,59] ΔQ is only -0.02 e^- in agreement with previous calculations based on AIM.[58]

Finally, we tested two helium clusters endofullerenes, He_6@C_{60} and He_{10}@C_{60}. Such systems are unlikely to exist in nature or to be synthesized, but can be used to investigate the influence on mechanical properties of the internal pressure built by helium atoms. Starting from a random configuration for He atoms, it is observed that He_6 quickly evolves towards a highly symmetric (O_h) structure (Fig. 1-c) during the calculation. For He_{10}, a low symmetry compact configuration is obtained (Fig. 1-d). Compared to a single NG atom, the binding energies are large and positive (Tab. 1), confirming that these compounds have little chances to be synthesized. Despite this large repulsion, it is remarkable that the C_{60} shell expansion remains limited, with dimensions increase of 0.017-0.019 and 0.07-0.08 Å respectively. This confirms that C_{60} is characterized by an outstanding structural resistance to high internal pressures.[7] Finally, we also determine excess charges of 0.13 and 0.19 e^- for He_6 and He_{10}, respectively.

The values of the Bader volume V_B at zero strain, calculated with the AIM method, are reported in Tab. 1. The comparison with the solid phase EOS volume V_0 indicates that the available volume for accommodating a molecule or atoms in the uncompressed C_{60} is about 20–22 $Å^3$. In fact, V_B is significantly reduced only for X with larger V_0. Therefore, only He and H_2O, and to a lesser extent Ne, can be considered to remain unconstrained when encapsulated into C_{60}. Our estimated "free" volume value is in agreement with an earlier study.[18] It also suggests that a physically good approximation of the C_{60} shell width is 3.4 Å.[60]

Table 1 Vinet EOS parameters for the atom or molecule X, and data for the endofullerene X@C_{60} computed at 300 K. V_0, B_0 and B_0' are the volume, bulk modulus, and bulk modulus derivative published values for X in solid phase: He,[44] Ne,[45] Ar,[46] Kr,[47] Xe,[48] H_2O,[49] CH_4.[50] V_0 for He_6 and He_{10} are the He value multiplied by the number of helium atoms. Δd_H and Δd_P are the length changes associated with the presence of X in C_{60} relatively to the empty fullerene, averaged at 300 K, with d_H (d_P) the separation between two facing hexagons (pentagons). V_B and ΔQ are the volume and excess charge of guest X at zero strain calculated using the Bader AIM analysis. ΔE is the binding energy of X in X@C_{60}, averaged at 300 K

	X Vinet EOS			X@C_{60} data				
X	V_0 (Å^3)	B_0 (GPa)	B_0'	Δd_H (Å)	Δd_P (Å)	V_B (Å^3)	ΔQ (e$^-$)	ΔE (eV)
He	11.476	0.537	6.928	+0.002	+0.000	12.7	+0.00	+0.082
He_6	68.856	0.537	6.928	+0.019	+0.017	34.9	+0.13	+3.401
He_{10}	114.76	0.537	6.928	+0.070	+0.081	44.6	+0.19	+10.585
Ne	22.234	1.070	8.40	+0.002	+0.001	16.1	+0.00	+0.027
Ar	38.0	2.65	7.423	+0.003	+0.003	24.3	-0.02	+0.196
Kr	54.813	1.55	7.10	+0.004	+0.003	24.3	-0.39	+0.054
Xe	57.407	4.887	6.296	+0.009	+0.007	31.4	-0.09	-0.381
H_2O	20.124	14.9	6.2	+0.001	+0.002	22.9	-0.02	0.000
CH_4	42.245	6.4	5.68	+0.005	+0.004	28.7	+0.00	-0.789

4 Mechanical properties of X@C_{60}

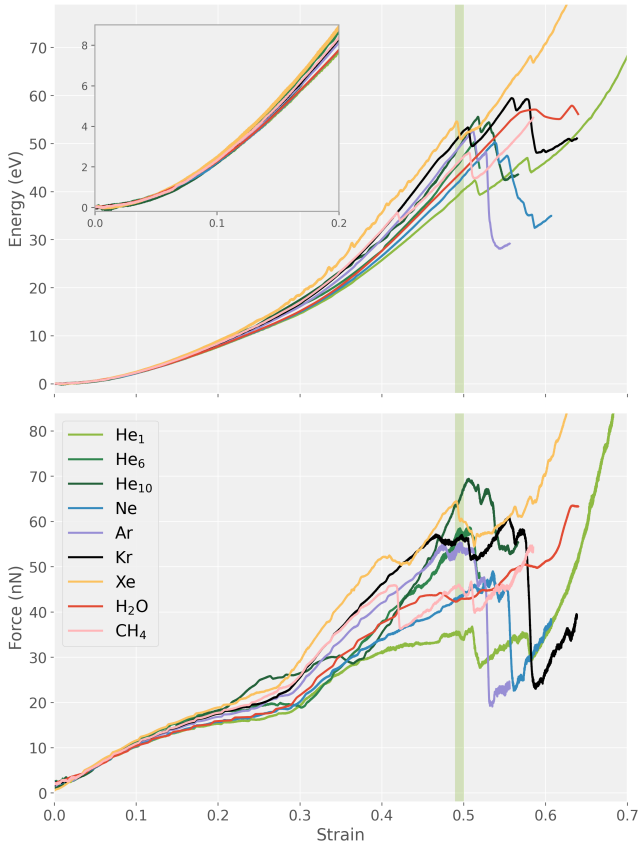

Fig. 2 Total energy (top graph, in eV) and contact force (bottom graph, in nN) as a function of compression strain for all studied endofullerenes. The energy reference is taken as the one of the uncompressed system at 300 K. The green strip lines show the strain range for which the first C–C bonds break for a bare C_{60}.[16] The top inset graph is a zoomed display of energy variations in the 0–0.2 strain range. Energy and force curves represented in separated graphs can be found in Supplementary Material.

In this section we focus on the mechanical properties of X@C_{60} compared to the known behavior for the "empty" C_{60}.[16] Figure 2 shows the total energy and contact force variations during the uniaxial compression of each studied systems. Most curves share similar characteristics. At low strains, the energy increases quadratically and the force linearly, as expected for an elastic regime. The slope of the force curve then decreases as compression proceeds, indicative of non-linear elasticity, up to strains equal to 0.27–0.30. This stage corresponds to the flattening of the two C_{60} azimuth caps in contact with the two repulsion force fields, in accordance with the predicted behavior for the bare C_{60}.[16] The various curves also tend to separate in this strain range, because of the growing specific influence of each guest X as compression proceeds. It is particularly significant for He_{10}@C_{60}, for which the contact force first grows steeper than for the others, for strains in the 0.20–0.26 range, then slower. This behavior is actually caused by a modification of the helium atoms packing (Fig. 3-(b-d)), as will be discussed in the following.

At strains equal to 0.3 the two caps are flattened, and force and energy variations become more steep for greater strain values. One or several maxima can be observed on both sets of curves, with clearly more features on force curves. All these maxima mark the activation of various mechanisms decreasing stress, contact force, and energy. A thorough structural analysis during compression reveals that these mechanisms correspond to changes either in the C_{60} shell or of the endohedral guest. For instance, the force maximum occurring at 0.40–0.41 strain followed by a small decrease for Xe@C_{60} (Fig. 2) is due to a reorientation of C_{60} relatively to the compression axis. The compression axis changes from pentagon center (Fig. 3-g) to bond center (Fig. 3-g). A different example is the force maximum at a strain of about 0.42 for CH_4@C_{60}, followed by a sharp drop (Fig. 2), which is caused by the dissociation of the CH_4 molecule.

We find that all force maxima occurring for strains in the range 0.48–0.58 are associated with the breaking of one or two carbon bonds in the equatorial part of the C_{60} shell, as for the bare fullerene.[16] For Kr@C_{60}, Ar@C_{60}, Ne@C_{60}, He_6@C_{60} and He_{10}@C_{60}, this is followed by the escape of one or several atoms through shell openings at slightly larger strains, leading to large force and energy drops (See Fig. 3-f,l for two examples). For the other systems, the molecule or the atom remains trapped in the defected shell. Note that in most cases, the compression simulation was stopped after the C_{60} shell opening. Only in the case of He@C_{60} the compression was continued up to a strain of 0.80 for which the complete C_{60} shell failure was observed. This strain threshold value is close to the one determined for the bare C_{60},[16]

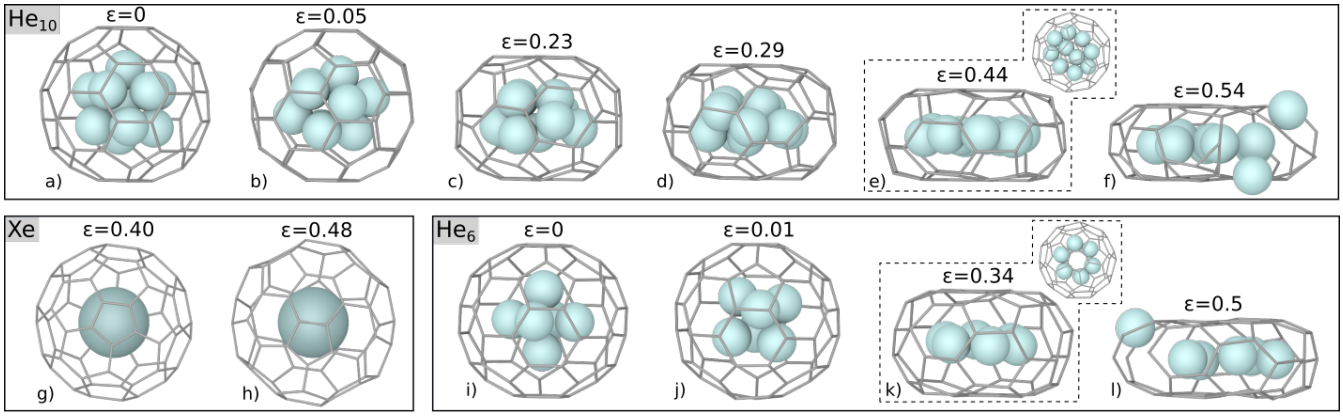

Fig. 3 Structures extracted from molecular dynamics calculations, at different compression strains, for $He_{10}@C_{60}$ (a-f), $Xe@C_{60}$ (g-h), and $He_6@C_{60}$ (i-l). For $He_{10}@C_{60}$ and $He_6@C_{60}$, the angle of view is perpendicular to the compression axis (side view), while for $Xe@C_{60}$ it is parallel (top view). For e) and k), an additional top right thumbnail picture shows a top view of the structure. Ball-and-stick representations are used for guests, while only the carbon bonds of the C_{60} host are shown for clarity.

although the helium atom remains always trapped.

Table 2 Data extracted from the compression of the endofullerene $X@C_{60}$ at 300 K: Stiffness S (N/m), yield strain ε_y determined from forces variations, force F_y (nN) and energy E_y (eV) at yield strain. Data for the empty C_{60}, computed with the same approach [16], are reported in the first line for comparison

X	S	ε_y	F_y	E_y
	155–157	0.49–0.51	30–32	36–40
He	155	0.49	36	42
He_6	167	0.49	58	50
He_{10}	157	0.51	69	56
Ne	156	0.52	48	50
Ar	162	0.49	54	53
Kr	164	0.48	56	53
Xe	176	0.49	64	54
H_2O	156	0.48	43	41
CH_4	166	0.51	46	48

To quantify the influence of X on the mechanical properties of $X@C_{60}$, we compute the stiffness S by fitting the energy curves with a quadratic function over a 0–0.1 strain range. We also determine the strain ε_y at which the C_{60} shell yields, i.e. the first carbon bond breaking, and the corresponding maximum force and energy values F_y and E_y. Data are reported in Table 2 and graphically in Fig. 4. In the latter, data are plotted as a function of V_0, the Vinet EOS volume of X (given in Tab. 1), assuming the latter quantity is a fair estimate of its initial volume. This is an arbitrary but convenient choice for the data visualization.

Figure 4 suggests that the stiffness is roughly proportional to V_0. However the increases relatively to the bare C_{60} remain small. The largest value, obtained for Xe, is for instance only 12% higher than the reference (green strips in Fig. 4). Note that the magnitude of the effect is comparable to stiffness variations associated with the orientation compression of a bare C_{60}. At the other end of the scale X with low V_0 such as He or H_2O have no noticeable influence on the stiffness. Eventually the only outlier is He_{10} for which S is the same than for the bare C_{60} despite a large V_0. This result might be explained by the initial dilation of $He_{10}@C_{60}$ before compression (quantified by Δd_H and Δd_P in Tab. 1). For

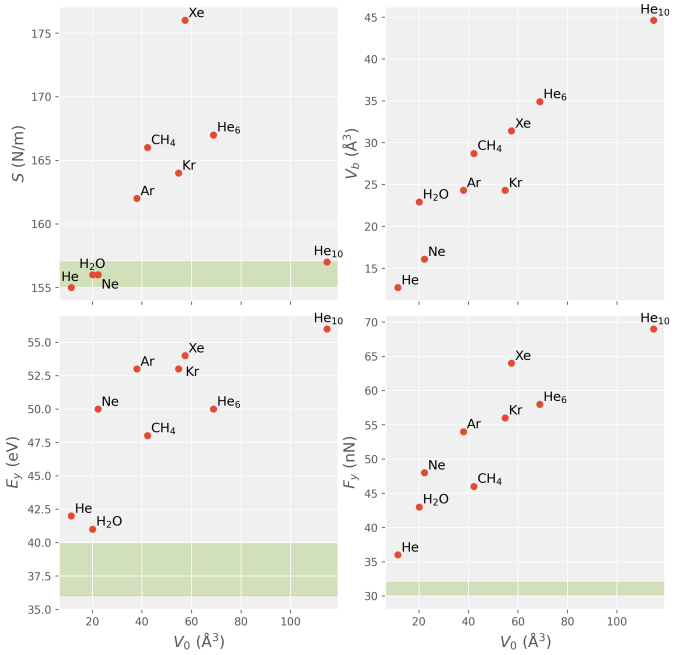

Fig. 4 Stiffness S (N/m), Bader volume V_B (Å^3), energy E_y (eV) and force F_y (nN) at yield, as a function of the Vinet volume V_0 (Å^3) for each $X@C_{60}$ system. The green strips show the range of values computed for a bare C_{60}, for the same orientation. [16]

small deformations, the compression reduces the initial C_{60} shell expansion, thus lowering the contact force increase rate and then the stiffness. This effect is partially compensated by the influence of He_{10}. Overall our observations suggest that the elastic behavior of the endofullerene is only weakly sensitive to the presence of the X guest, and depends essentially on the C_{60} shell. This is not surprising if one compares for instance the large differences in elastic moduli between fullerenes [61] and noble gas. [62]

We now analyze data related to the yield point, i.e. the yield strain ε_y, the energy E_y and force F_y. ε_y is not represented in Fig. 4 since this quantity is obviously not correlated to V_0 (Tab. 2). Note

that there is an estimated 1–2% uncertainty in the determination of ε_y, because of the sluggish breaking of the first carbon bond and the potential error in the 0% definition. Nevertheless variations remain small and in the stochastic range of values computed for the bare C_{60}.[16] Also, we find that the plasticity mechanisms are the same in all cases. This means that the presence of X and its nature have little influence on the strain at which plasticity in the C_{60} shell is initiated, at least for the various tested systems.

On the contrary one can see that X greatly influences both energy and contact force at the yield point, and that the variations are roughly proportional to V_0 (Fig. 4). The energy increase compared to the bare C_{60} is equal to a few eV for He and H_2O, and can be as large as 16–20 eV for He_{10}. For the contact force, we determine increments of at least 4–6 nN for He, and up to 37–39 nN for He_{10} i.e., more than twice the bare C_{60} value. Both energy and contact force are then highly dependent on X. This is probably because the onset of plasticity occurs at high strain values where both the C_{60} shell and X are compressed. The contributions of X to the energy and contact force then become significant in this strain regime. They also appear to be roughly proportional to the initial volume V_0, although the compressibility of X might be influential as well.

5 Properties of X in compressed X@C_{60}

5.1 Volume, pressure, and charge transfer

Now we analyze how the properties of the atoms or of the molecule encapsulated in C_{60} are modified by the compression. Figure 5 shows the variations of the volume V_B for each X content, calculated with the AIM method. All curves are characterized by similar features. V_B decreases slowly at low strains and with an increasing rate as compression proceeds. This behavior is in agreement with our previous statement that at low strains, the mechanical properties of X@C_{60} are weakly influenced by the presence of X. The sole exception is He_{10}, for which V_B tends to decrease almost linearly from the start of the compression. In all cases the steep volume increase for strains greater than 0.5 is due to X or a part of X escaping through the broken C_{60} shell. Examples of such processes are represented in Fig. 3-f,l.

Using the EOS for the various X systems, one can estimate the pressure variation associated with the volume decrease. Obviously, the notion of pressure in the case of a single atom or molecule is conceptual and has to be considered with caution. Furthermore, the stress inside a uniaxially compressed C_{60} is likely to be not hydrostatic. We argue that this pressure estimation is nonetheless useful to get insights on the state of the C_{60} guest during the compression. Computed pressure variations during compression are shown in Fig. 5. For most X@C_{60} systems, the pressure first increases slowly, then faster after a given compression level. The inflection occurs at a strain value of about 0.4 for the biggest X (Kr, Xe) up to about 0.45 for the smallest ones (He, Ne, H_2O). It corresponds to X being effectively compressed between the two flattened C_{60} caps. The situation is different for He_6, He_{10} and to a lesser extent CH_4, for which no clear inflection is obtained. This is because the structure of the clusters and of the molecule continuously changes during compression in

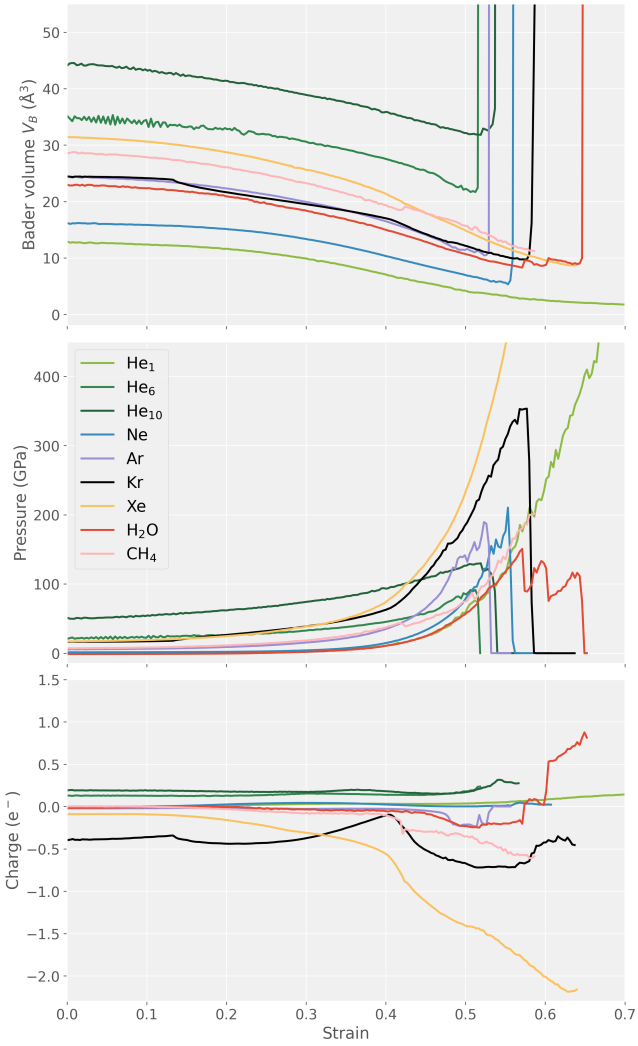

Fig. 5 Bader volume V_B (top graph, in Å^3), atomic pressure (middle graph, in GPa), and charge transfer ΔQ (bottom graph, in e$^-$) of X as a function of strain during the compression of X@C_{60}. V_B and ΔQ are computed using the AIM approach. A positive ΔQ value corresponds to an electron transfer from C_{60} to X. The pressure is derived from the computed volume using the appropriate EOS at 300 K for each X.

order to better accommodate the stress. For instance, the initial three-dimensional packing of He_{10} is progressively transformed to a two-dimensional helium layer (Fig. 3-(a-e)). Similarly He_6 departs from its initial structure (Fig. 1-c) to a seemingly HCP packing at very low strain (Fig. 3-j), which is next gradually converted to a single helium layer (Fig. 3-(k)).

Maximal pressure values of 91 GPa (He_6), 130 GPa (He_{10}), 210 GPa (Ne), 189 GPa (Ar), 353 GPa (Kr) are determined (Fig. 5). For H_2O and CH_4, the maximum values for an undissociated molecule are 151 GPa and 44 GPa, respectively. Finally, we also found extremely high pressures of 985 GPa for Xe and 731 GPa for He, the later corresponding to a strain of 0.75. Although these values must be considered with caution, this suggests that single atoms or small molecules in a very high stress state could be achieved, provided of course that the controlled compression at high strain of C_{60} and endofullerenes would be

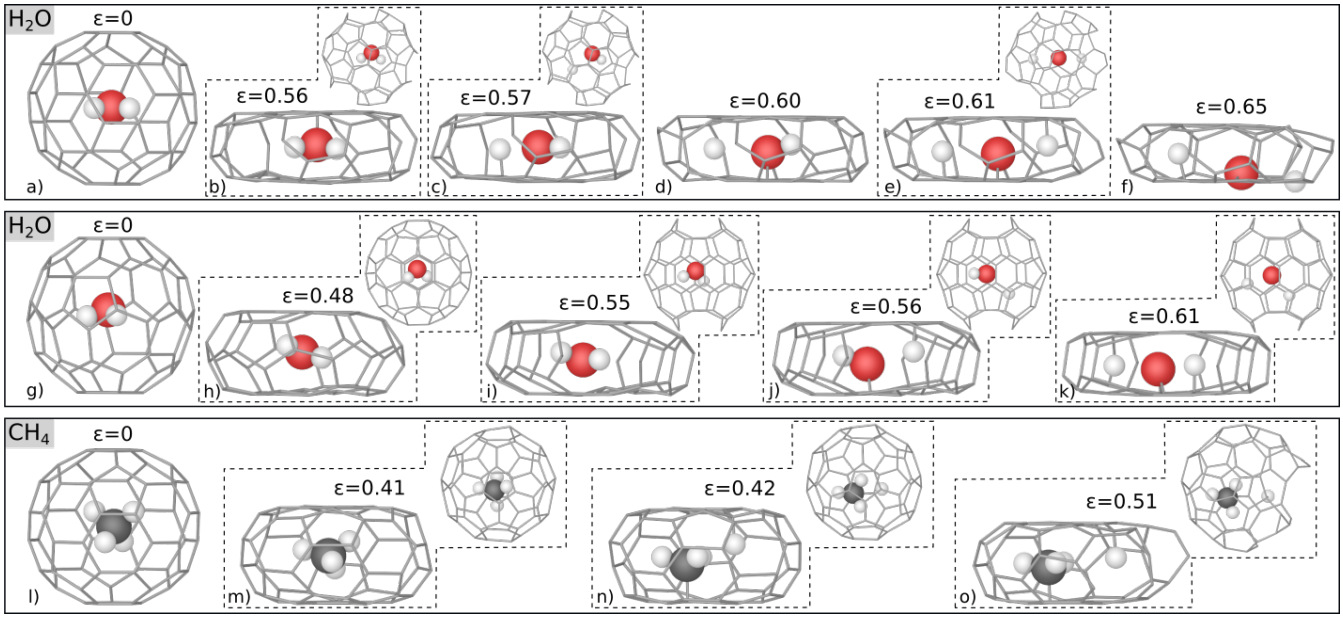

Fig. 6 Structures extracted from molecular dynamics calculations, at different strains, for $H_2O@C_{60}$ compressed along pentagon-pentagon (a-f) and hexagon-hexagon (h-k) orientations, and for $CH_4@C_{60}$ (l-o). The angle of view is perpendicular to the compression axis (side view). For selected strains, an additional top right thumbnail picture shows a top view of the structure. Ball-and-stick representations are used for guests, while only the carbon bonds of the C_{60} host are shown for clarity.

made possible in the future.

The charge variations ΔQ for each X, determined using AIM during the compression of $X@C_{60}$, are shown in Figure 5. For strains below 0.48 i.e., before yielding of the C_{60} shell, values tend to remain small and weakly dependent on strain for the smallest noble gas atoms like He, Ne and Ar. Larger charge transfers are observed for He_6 and He_{10}, but they remain low with a maximum of 0.2 e^- in excess in helium clusters. A surprisingly high electron deficit is determined for Kr, but it is difficult to determine a rationale for variations as a function of strain. By comparison, Xe is characterized by a low electron deficit of 0.09 at zero strain, this value increasing with the compression strain. We determine a maximum electron deficit of 2.2 e^- from Xe to C_{60} at $\varepsilon = 0.63$. For H_2O and CH_4 molecules, the small initial electron transfer to the C_{60} shell increases as compression proceeds. Hence ΔQ for H_2O decreases to a minimum of -0.25 e^- at $\varepsilon = 0.51$. Figure 5 shows that for higher strains ΔQ increases sharply to positive values. However it now corresponds to a dissociated molecule as will be described in the following section. In the case of CH_4, the electron deficit in the molecule grows with the compression strain, with a value of -0.1 e^- at $\varepsilon = 0.41$. Contrary to H_2O, δQ continues to decrease for larger strain values and after molecular transformation, down to a minimum value of -0.6.

5.2 Compression-assisted chemical transformations

It has been proposed that the compression of $H_2O@C_{60}$ or $CH_4@C_{60}$ could lead to the formation of endohedral covalent derivatives.[19,20] In this section, we examine the evolution of H_2O and CH_4 inside C_{60} during the compression to determine whether such mechanisms occur in our calculations.

Considering first H_2O, we observe that at very low strains the molecule could rotate slowly almost freely in all directions while remaining in the C_{60} center. Increasing the strain suppresses the rotation, with the molecule contained in the plane perpendicular to the compression axis (Fig. 6-a). The O–H bonds lengths and the $\widehat{HOH}$ angle remain constant in average with respective values of 0.972 Å and 104.4° until $\varepsilon = 0.47$. Next they increase up to maximum values of 1.078 Å and 110.0° at $\varepsilon = 0.56$, while the oxygen atom gets closer to the nearest carbon atoms in the C_{60} shell (Fig. 6-b). The AIM analysis shows that the two H atoms have each a deficit of 0.6 e^-, and the C atom an excess of 1.0 e^- in average. At $\varepsilon = 0.57$, one hydrogen atom separates from the oxygen and forms a C–H bond with a C_{60} shell atom (Fig. 6-c). Its charge deficit is reduced to about 0.2 e^-, and the O excess charge becomes 0.9 e^-. It corresponds to an electron deficit of 0.1 e^- in C_{60}. For these compression strains, the separation between top and bottom flattened C_{60} caps becomes small enough to consider that the remaining hydroxide ion interacts with the two closest top and bottom shell carbon atoms. Also, the lone hydrogen atom seems to form short lifetime bonds alternatively with a top and a bottom C atom. At $\varepsilon = 0.60 - 0.61$, we observe the formation of an epoxide group (Fig. 6-d), followed by the separation of the second H atom from O and the formation of a C–H bond (Fig. 6-e). This H atom exhibits a charge deficit of 0.2 e^-, like for the first hydrogen atom. The epoxide group is characterized by C–O bond lengths of 1.3–1.4 Å and a C–C bond length of 1.55 Å. The charge is in excess of 1.05 e^- on the O atom, and in deficit of about 0.35 e^- on these two C atoms. Finally, as compression proceeds, this C–C bond progressively breaks which triggers the fracture of C_{60} and the escape of the oxygen and of one hydrogen through the created hole (Fig. 6-f). A movie showing the $H_2O@C_{60}$ compression is available in the Supplementary Material.

Sabirov and co-workers reported a similar dissociated H_2O configuration at a strain of 0.58, with the formation of an epoxide group and two remote C–H bonds.[19] The excellent agreement with the present work is impressive given that our methodology for computing electronic structure and applying compression is different, and also that their simulations are done at 0 K. In the same study the authors also investigated the uniaxial compression of $H_2O@C_{60}$ for an hexagon–hexagon orientation. They reported a full dissociation of H_2O into an oxidoannulene structure and two single C–H bonds, at a strain of 0.57, with therefore an apparently different mechanism than for the pentagon–pentagon compression.[19] To compare with these findings, we also carried out 300 K MD simulations of the $H_2O@C_{60}$ compression for this orientation. Our results are shown in Fig. 6-(g-k). Up to $\varepsilon = 0.55$, the H_2O molecule is observed to remain in the center of C_{60}, a difference with the previous case being that it is tilted relatively to the compression plane (Fig. 6-h). At this strain the O atom carries an excess charge of about 1.0 e^-, and the H atoms a deficit of 0.2 e^-, similar to what is obtained for the pentagon–pentagon orientation. Note that at this strain the C_{60} shell is already opened with no incidence on the molecule state (Fig. 6-i). When $\varepsilon = 0.56$, one hydrogen atom loosens and moves to make a bond with the C_{60} shell (Fig. 6-j). The remaining hydroxide ion also binds to C_{60}, first with a single bond, then as an epoxide group after a few extra tenths of strain. Its charge is now approximately +0.4 e^- (+1.0 e^- for O and -0.6 e^- for H), while the lone H atom carries a charge of -0.2 e^-. When $\varepsilon = 0.61$ the H–O bond breaks, the hydrogen atom moving to make a bond with C_{60} (Fig. 6-k). At this strain, we find a charge deficit of 0.2 e^- for both hydrogen atoms, and a charge excess of 0.4 e^- for the oxygen atom. Increasing the compression leads to the breaking of the bond between the two carbon atoms bonded to the oxygen atom, and then the failure of the C_{60} shell. Finally the whole process is qualitatively and quantitatively similar to what we find for the pentagon–pentagon compression. This suggests that the seemingly different behaviors reported by Sabirov and co-workers[19] for the two compression orientations likely result from the use of large strain increments, preventing a detailed analysis of the structural transformations. It also confirms that it is possible to achieve a full dissociation of a single H_2O molecule when encapsulated into a compressed fullerene.

Finally we also find that the compression of $CH_4@C_{60}$ triggers a chemical transformation (see the Supplementary Material for a movie). Initially, the CH_4 molecule is only weakly perturbed, with C–H bond lengths of about 1.1 Å and $\widehat{HCH}$ angles close to the expected value of 109.5° (Fig. 6-l). The carbon atom carries approximately 0.4 e^- in excess, whereas the hydrogen atoms are characterized by a charge deficit of 0.1 e^-. As compression proceeds, the C–H bonds shorten to 1.07 Å and the $\widehat{HCH}$ angles including the two top or the two bottom H atoms rise to a maximum of 133° at $\varepsilon = 0.41$ (Fig. 6-m). In parallel there is a small 0.1 e^- transfer from CH_4 to C_{60}. At $\varepsilon = 0.42$, the topmost H atom separates from the molecule C atom to form a bond with C_{60}, and the remaining methyl radical binds to the C_{60} shell (Fig. 6-n). Associated energy and force reductions of 1.7 eV and 9.3 nN are calculated (Fig. 2). This mechanism implies a 0.2 e^- transfer from the molecule carbon atom to C_{60}, but no appreciable charge changes for the hydrogen atoms. Increasing the strain weakly reduces the bond lengths for the lone hydrogen and the methyl group. The excess charge on C_{60} and on the C atom increase to 0.55–0.6 e^-, whereas for the H atoms the charge deficit rises to 0.3 e^-. At $\varepsilon = 0.51$, the C_{60} shell yields by the breaking of carbon bonds in the equatorial region (Fig. 6-o), with no clear direct relation with the presence of the methyl group and the single hydrogen atom. Finally, we note that the carbon atom in CH_3 binds to a second C_{60} shell atom at approximately $\varepsilon = 0.55$, before we stop the compression. The process as a whole appears to be similar to an earlier prediction.[20] In this latter study, the strain at which the $CH_4 \rightarrow CH_3 + H$ transformation takes place is reported to be 0.40, therefore in excellent agreement with the present value of 0.42.

6 Conclusions

In this study the mechanical properties of various kinds of endofullerenes $X@C_{60}$ were investigated by performing first principles molecular dynamics simulations of uniaxial compression over a large strain range. We considered realistic and synthesizable X systems, including single noble gas atoms, H_2O or CH_4 molecules, as well as artificial helium clusters. These calculations and the associated analyses lead to the following conclusions:

- In the absence of strain, it is confirmed that the interactions between X and C_{60} are weak in most cases, with negligible modifications of structural properties and limited charge transfers. A light expansion of the C_{60} shell was obtained only in the case of encapsulated helium clusters.
- In the elastic regime an increase of stiffness, proportional to the intrinsic volume of X, is predicted. However this increase is at most 12% of the C_{60} stiffness.
- The presence or the nature of X has no noticeable influence on the yield strain and on the C_{60} shell yielding mechanisms. Still the variations of both the contact force and the energy clearly depend on X. For instance large increases of their values at yield are predicted.
- The estimation of the volume of X and of a derived pressure shows that single noble gas atoms and small molecules could be put in a very high stress state, with pressure values in the range 50–200 GPa, during the compression of endofullerenes.
- The simulations confirm that the uniaxial compression could trigger the dissociation of H_2O or CH_4 when these molecules are encapsulated into C_{60}.

To summarize, the uniaxial compression of $X@C_{60}$ is predicted to have a strong effect on the properties of X, but a rather limited one on the mechanical properties of C_{60}. This is mainly a consequence of our choice of closed-shell atoms or molecules for X, for which electronic interactions with the C_{60} shell are minimal. A natural an interesting continuation of this work would then be to consider endohedral metallofullerenes, where one or two metal atoms are enclosed in a fullerene.[1] The usually strong interaction

of these atoms with the fullerene shell is likely to influence its mechanical strength and yield mechanisms, defining a research topic worth to be explored.

Conflicts of interest

There are no conflicts to declare.

Acknowledgements

The computer time for this work was provided by several sources: the Spin Center at the University of Poitiers, the MCIA (Mésocentre de Calcul Intensif Aquitain), and GENCI-CINES (Grant 2020-A0090912035).

Notes and references

1 *Endofullerenes*, ed. T. Akasaka and S. Nagase, Springer Netherlands, 2002, vol. 3.

2 P. W. Dunk, J.-J. Adjizian, N. K. Kaiser, J. P. Quinn, G. T. Blakney, C. P. Ewels, A. G. Marshall and H. W. Kroto, *Proc. Nat. Acad. Sci.*, 2013, **110**, 18081–18086.

3 H. Shinohara and N. Tagmatarchis, *Endohedral Metallofullerenes: Fullerenes with Metal Inside*, Wiley, United Kingdom, 2015.

4 M. Saunders, H. A. Jiménez-Vázquez, R. J. Cross and R. J. Poreda, *Science*, 1993, **259**, 1428–1430.

5 M. Saunders, H. A. Jimenez-Vazquez, R. J. Cross, S. Mroczkowski, M. L. Gross, D. E. Giblin and R. J. Poreda, *J. Am. Chem. Soc.*, 1994, **116**, 2193–2194.

6 M. Saunders, R. J. Cross, H. A. Jiménez-Vázquez, R. Shimshi and A. Khong, *Science*, 1996, **271**, 1693–1697.

7 S. Jalife, J. Arcudia, S. Pan and G. Merino, *Chem. Sci.*, 2020, **11**, 6642–6652.

8 K. Kurotobi and Y. Murata, *Science*, 2011, **333**, 613–616.

9 S. Bloodworth, G. Sitinova, S. Alom, S. Vidal, G. R. Bacanu, S. J. Elliott, M. E. Light, J. M. Herniman, G. J. Langley, M. H. Levitt and R. J. Whitby, *Angew. Chem. Int. Ed.*, 2019, **58**, 5038–5043.

10 S. Bloodworth, G. Hoffman, M. C. Walkey, G. R. Bacanu, J. M. Herniman, M. H. Levitt and R. J. Whitby, *Chemical Communications*, 2020, **56**, 10521–10524.

11 D. Brenner, J. Harrison, C. White and R. Colton, *Thin Solid Films*, 1991, **206**, 220–223.

12 G. Galli and F. Mauri, *Phys. Rev. Lett.*, 1994, **73**, 3471–3474.

13 Z. Wang, K. Su, H. Fan, L. Hu, X. Wang, Y. Li and Z. Wen, *Comp. Mat. Sci.*, 2007, **40**, 537–547.

14 K.-J. Seo and D.-E. Kim, *Nanoscale*, 2020, **12**, 9849–9858.

15 L. Pizzagalli, *Phys. Rev. B*, 2020, **102**, 094102.

16 L. Pizzagalli, *Diamond & Related Materials*, 2022, **123**, 108870.

17 R. D. Beck, P. S. John, M. M. Alvarez, F. Diederich and R. L. Whetten, *J. Phys. Chem.*, 1991, **95**, 8402–8409.

18 P. Delaney and J. C. Greer, *Appl. Phys. Lett.*, 2004, **84**, 431–433.

19 D. S. Sabirov, *J. Phys. Chem. C*, 2013, **117**, 1178–1182.

20 D. S. Sabirov, A. A. Tukhbatullina and R. G. Bulgakov, *Fullerenes, Nanotubes and Carbon Nanostructures*, 2015, **23**, 835–842.

21 J. R. Greer and J. T. D. Hosson, *Progress in Materials Science*, 2011, **56**, 654 – 724.

22 T. Pardoen, M.-S. Colla, H. Idrissi, B. Amin-Ahmadi, B. Wang, D. Schryvers, U. K. Bhaskar and J.-P. Raskin, *Comptes Rendus Physique*, 2016, **17**, 485–495.

23 J. Sun, L. He, Y.-C. Lo, T. Xu, H. Bi, L. Sun, Z. Zhang, S. X. Mao and J. Li, *Nature Materials*, 2014, **13**, 1007–1012.

24 A. J. Wagner, E. D. Hintsala, P. Kumar, W. W. Gerberich and K. A. Mkhoyan, *Acta Mater.*, 2015, **100**, 256 – 265.

25 E. Hintsala, A. Wagner, W. Gerberich and K. Mkhoyan, *Scripta Materialia*, 2016, **114**, 51 – 55.

26 M. T. Kiani, Y. Wang, N. Bertin, W. Cai and X. W. Gu, *Nanoletters*, 2019, **19**, 255–260.

27 I. Z. Jenei, F. Dassenoy, T. Epicier, A. Khajeh, A. Martini, D. Uy, H. Ghaednia and A. Gangopadhyay, *Tribology International*, 2019, **131**, 446–453.

28 R. Pawlak, S. Kawai, S. Fremy, T. Glatzel and E. Meyer, *ACS Nano*, 2011, **5**, 6349–6354.

29 S. P. Jarvis, H. Sang, F. Junqueira, O. Gordon, J. E. A. Hodgkinson, A. Saywell, P. Rahe, S. Mamone, S. Taylor, A. Sweetman, J. Leaf, D. A. Duncan, T.-L. Lee, P. K. Thakur, G. Hoffman, R. J. Whitby, M. H. Levitt, G. Held, L. Kantorovich, P. Moriarty and R. G. Jones, *Communications Chemistry*, 2021, **4**, 135.

30 J. Amodeo and L. Pizzagalli, *Comptes Rendus Physique*, 2021, **22**, 1–32.

31 R. Car and M. Parrinello, *Phys. Rev. Lett.*, 1985, **55**, 2471.

32 P. Giannozzi, O. Andreussi, T. Brumme, O. Bunau, M. B. Nardelli, M. Calandra, R. Car, C. Cavazzoni, D. Ceresoli, M. Cococcioni, N. Colonna, I. Carnimeo, A. D. Corso, S. de Gironcoli, P. Delugas, R. A. DiStasio, A. Ferretti, A. Floris, G. Fratesi, G. Fugallo, R. Gebauer, U. Gerstmann, F. Giustino, T. Gorni, J. Jia, M. Kawamura, H.-Y. Ko, A. Kokalj, E. Küçükbenli, M. Lazzeri, M. Marsili, N. Marzari, F. Mauri, N. L. Nguyen, H.-V. Nguyen, A. O. de-la Roza, L. Paulatto, S. Poncé, D. Rocca, R. Sabatini, B. Santra, M. Schlipf, A. P. Seitsonen, A. Smogunov, I. Timrov, T. Thonhauser, P. Umari, N. Vast, X. Wu and S. Baroni, *J. Phys.: Condens. Matter*, 2017, **29**, 465901.

33 F. Tassone, F. Mauri and R. Car, *Phys. Rev. B*, 1994, **50**, 10561–10573.

34 P. Hohenberg and W. Kohn, *Phys. Rev.*, 1964, **136**, B864–B871.

35 W. Kohn and L. J. Sham, *Phys. Rev.*, 1965, **140**, A1133–A1138.

36 J. P. Perdew, K. Burke and M. Ernzerhof, *Phys. Rev. Lett.*, 1996, **77**, 3865–3868.

37 D. Vanderbilt, *Phys. Rev. B*, 1990, **41**, 7892–7895.

38 C. S. Yannoni, P. P. Bernier, D. S. Bethune, G. Meijer and J. R. Salem, *Journal of the American Chemical Society*, 1991, **113**, 3190–3192.

39 D. Kilymis, C. Gérard, J. Amodeo, U. Waghmare and L. Pizzagalli, *Acta Mater.*, 2018, **158**, 155–166.

40 R. Bader, *Atoms in Molecules: A Quantum Theory*, Oxford University Press, New York, 1990.

41 A. O. de-la Roza, E. R. Johnson and V. Luaña, *Comput. Phys. Commun.*, 2014, **185**, 1007–1018.

42 P. E. Blöchl, C. G. van de Walle and S. T. Pantelides, *Phys. Rev. Lett.*, 1990, **64**, 1401.

43 M. Yu and D. R. Trinkle, *The Journal of Chemical Physics*, 2011, **134**, 064111.

44 P. Loubeyre, R. LeToullec, J. P. Pinceaux, H. K. Mao, J. Hu and R. J. Hemley, *Phys. Rev. Lett.*, 1993, **71**, 2272.

45 A. Dewaele, F. Datchi, P. Loubeyre and M. Mezouar, *Phys. Rev. B*, 2008, **77**, 094106.

46 A. Dewaele, A. D. Rosa, N. Guignot, D. Andrault, J. E. F. S. Rodrigues and G. Garbarino, *Scientific Reports*, 2021, **11**, 15192.

47 A. D. Rosa, G. Garbarino, R. Briggs, V. Svitlyk, G. Morard, M. A. Bouhifd, J. Jacobs, T. Irifune, O. Mathon and S. Pascarelli, *Phys. Rev. B*, 2018, **97**, 094115.

48 A. Dewaele, P. Loubeyre, P. Dumas and M. Mezouar, *Phys. Rev. B*, 2012, **86**, 014103.

49 E. Wolanin, P. Pruzan, J. C. Chervin, B. Canny, M. Gauthier, D. Häusermann and M. Hanfland, *Phys. Rev. B*, 1997, **56**, 5781–5785.

50 L. Sun, Z. Zhao, A. L. Ruoff, C.-S. Zha and G. Stupian, *J. Phys.: Condens. Matter*, 2007, **19**, 425206.

51 N. N. Breslavskaya and A. L. Buchachenko, *Fullerenes, Nanotubes and Carbon Nanostructures*, 2004, **12**, 47–52.

52 R. Sure, R. Tonner and P. Schwerdtfeger, *J. Comput. Chem.*, 2015, **36**, 88–96.

53 R. B. Darzynkiewicz and G. E. Scuseria, *J. Phys. Chem. A*, 1997, **101**, 7141–7144.

54 S. Grimme, *J. Comput. Chem.*, 2006, **27**, 1787–1799.

55 A. Rehaman, L. Gagliardi and P. Pyykkö, *Int. J. Quantum Chem.*, 2007, **107**, 1162–1169.

56 A. Galano, A. Pérez-González, L. del Olmo, M. Francisco-Marquez and J. R. León-Carmona, *J. Mol. Modeling*, 2014, **20**, 2412.

57 C. Ramachandran and N. Sathyamurthy, *Chem. Phys. Lett.*, 2005, **410**, 348–351.

58 A. Varadwaj and P. R. Varadwaj, *Chem. Eur. J.*, 2012, **18**, 15345–15360.

59 O. Carrillo-Bohórquez, Á. Valdés and R. Prosmiti, *J. Chem. Theory Comput.*, 2021, **17**, 5839–5848.

60 C. Y. Wang and L. C. Zhang, *Nanotechnology*, 2008, **19**, 075705.

61 S. Woo, S. H. Lee, E. Kim, K. Lee, Y. H. Lee, S. Y. Hwang and I. C. Jeon, *Phys. Lett. A*, 1992, **162**, 501–505.

62 L. Pizzagalli, A. Charaf-Eddin and S. Brochard, *Comp. Mat. Sci.*, 2014, **95**, 149 – 158.